A MEASUREMENT OF SEMI INCLUSIVE DEEP INELASTIC SCATTERING PION ASYMMETRIES

T. Didberidze and T. Forest

Department of Physics, Idaho State University, Pocatello, ID 83201, USA

June 6, 2013

Abstract

Semi-inclusive deep inelastic scattering (SIDIS) experiments may be used to identify the flavor of the quark that participates in the scattering process. Semi-inclusive scattering is defined as an electron scattering experiment in which the scattered electron and one hadron are detected in the final state. Experiments at Jefferson Lab have used longitudinally polarized electrons to probe longitudinally polarized Hydrogen ($^{15}NH_3$) and Deuterium ($^{15}ND_3$) targets and investigate the quark's contribution to the nucleon properties. This work reports a measurement of SIDIS pion asymmetries using the CEBAF Large Acceptance Spectrometer (CLAS) at Thomas Jefferson National Laboratory. The incident electron's energy was 4.2 GeV and covered a kinematic region where the struck quark carries at least 30% of the nucleons total momentum ($x_B \geq 0.3$). The electrons scatter mostly from valence quarks in this kinematic region allowing measurements which are less sensitive to the ocean of quark-antiquark pairs that are also inside a nucleon.

Table of Contents

List of Figures

List of Tables

Chapter 1

Data Analysis

Semi-inclusive deep inelastic scattering (SIDIS) experiments using longitudinally polarized hydrogen ($^{15}NH_3$) and deuterium ($^{15}ND_3$) targets and a longitudinally polarized electron beam can be used to measure the ratio of the polarized valence quark distribution function to the unpolarized ($\Delta q/q$). Semi-inclusive scattering identifies an electron scattering experiment in which the scattered electron and one hadron are detected in the final state. This chapter describes the techniques used to analyze the data collected during the EG1b experiment and calculate semi-inclusive asymmetries for the following reactions: $\vec{e}^{-}\vec{N} \rightarrow e^{-}\pi^{+}X$ and $\vec{e}^{-}\vec{N} \rightarrow e^{-}\pi^{-}X$ using NH_3 and ND_3 polarized targets respectively. The goal of this work is to measure charged pion asymmetries defined according to the incident electron helicity and the target polarization. This work focuses on a kinematic region where the struck quark carries at least 30% of the nucleons total momentum ($x_b > 0.3$). The leptons scatter mostly from valence quarks in this kinematic region allowing contributions from sea quarks to be neglected. SIDIS measurements are able to distinguish between the predictions made by the hyperfine perturbed constituent quark model (pCQM) and perturbative Quantum Chromodynamics (pQCD).

1.1 The CLAS Data Selection

The data files from the EG1b experiment chosen for this analysis are listed in Table 1.1. During the experiment, 2.2 GeV, 4.2 GeV and 5.7 GeV longitudinally polarized electron beams were used to probe the polarized NH_3 and ND_3 targets. This work will discuss the analysis of the 4.2 GeV electron beam data set as this energy provided the most statistics. The restrictions applied to the reconstructed events are described below.

Run Set	Target Type	Torus Current(A)	Target Polarization	HWP
28100 - 28102	ND_3	+2250	-0.18	+1
28106 - 28115	ND_3	+2250	-0.18	-1
28145 - 28158	ND_3	+2250	-0.20	+1
28166 - 28190	ND_3	+2250	+0.30	+1
28205 - 28217	NH_3	+2250	+0.75	+1
28222 - 28236	NH_3	+2250	-0.68	+1
28242 - 28256	NH_3	+2250	-0.70	-1
28260 - 28275	NH_3	+2250	+0.69	-1
28287 - 28302	ND_3	-2250	+0.28	+1
28306 - 28322	ND_3	-2250	-0.12	+1
28375 - 28399	ND_3	-2250	+0.25	-1
28407 - 28417	NH_3	-2250	+0.73	-1
28456 - 28479	NH_3	-2250	-0.69	+1

Table 1.1: EG1b runs analyzed for this work.

1.2 Particle Identification

The sections below describe the additional tests performed on the electron and pion candidates reconstructed by the standard CLAS software package (RECSIS). Electrons are identified by matching the charged particle hits in

the drift chamber (DC), Cherenkov counter (CC), electromagnetic calorimeter (EC), and the time of flight (ToF) system [1]. Geometrical and timing cuts are applied to improve electron identification [2]. In addition, cuts are applied on the energy deposited by the particle into the calorimeter and the number of photoelectrons produced in the Cherenkov counter. Charged pions are identified by matching the hits in the drift chamber and ToF counter, along with a Cherenkov cut requiring that the number of photons for pions be less than two.

1.2.1 Electron Identification

The CLAS trigger system required a particle to deposit energy in the electromagnetic calorimeter and illuminate the Cherenkov counter within a 150 ns time window (Figure 1.1). Unfortunately, this trigger suffers from a background of high energy negative pions that may be misidentified as electrons. The pion contamination of the electron sample is reduced using cuts on the energy deposited in the electromagnetic calorimeter and the momentum measured by reconstructing the particle's track in the known magnetic field. The energy deposition mechanism for pions and electrons in the electromagnetic calorimeter is different. The total energy deposited by the electrons in the EC is proportional to their kinetic energy, whereas pions are minimum ionizing particles and the energy deposition is independent of their momentum (Figure 1.2). The pion background is further suppressed using geometrical and time matching cuts between the Cherenkov counter hit and the measured track in the drift chamber.

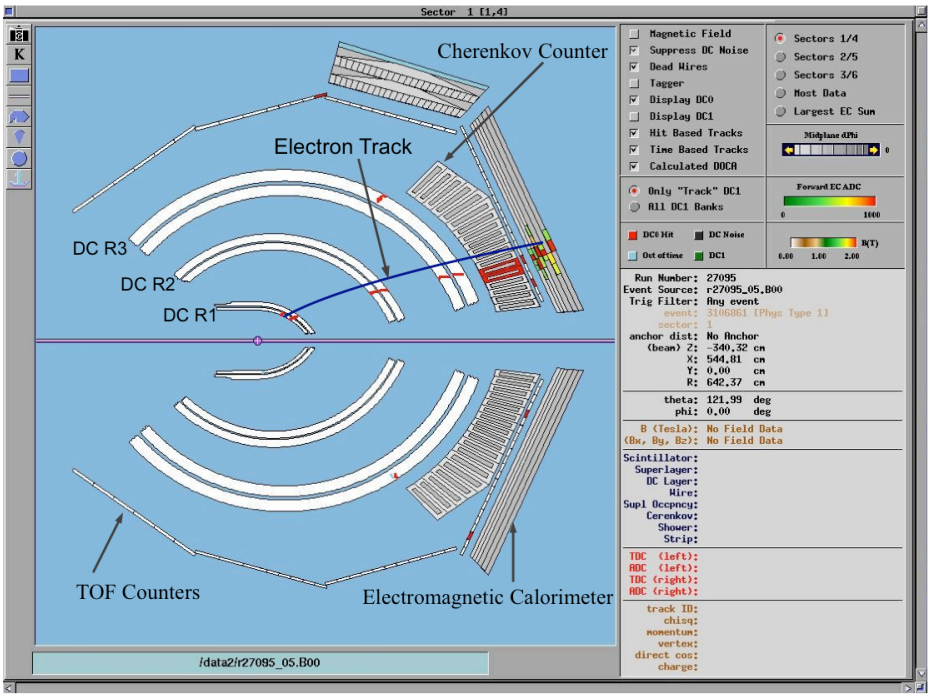

Fig. 1.1: Example of an electron candidate passing through the drift chambers and creating the signal in the Cherenkov counter and electromagnetic calorimeter. The electron track is highlighted by the blue line (Run number 27095, Torus Current +2250 (inbending)).

EC CUTS

The CLAS electromagnetic calorimeter was used to reduce the misidentification of electron and negative pion candidates. The electromagnetic calorimeter contains thirteen layers of lead-scintillator sandwiches composed of $\sim$ 2 mm thick lead and 10 mm thick scintillator. Each set of thirteen layers is subdivided into five inner and eight outer layers that are named the inner and outer calorimeter respectively.

Electrons interact with the calorimeter producing electromagnetic showers that release energy into the calorimeter. The deposited energy is proportional to the momentum of the electrons. Figure 1.3 shows the correlation of

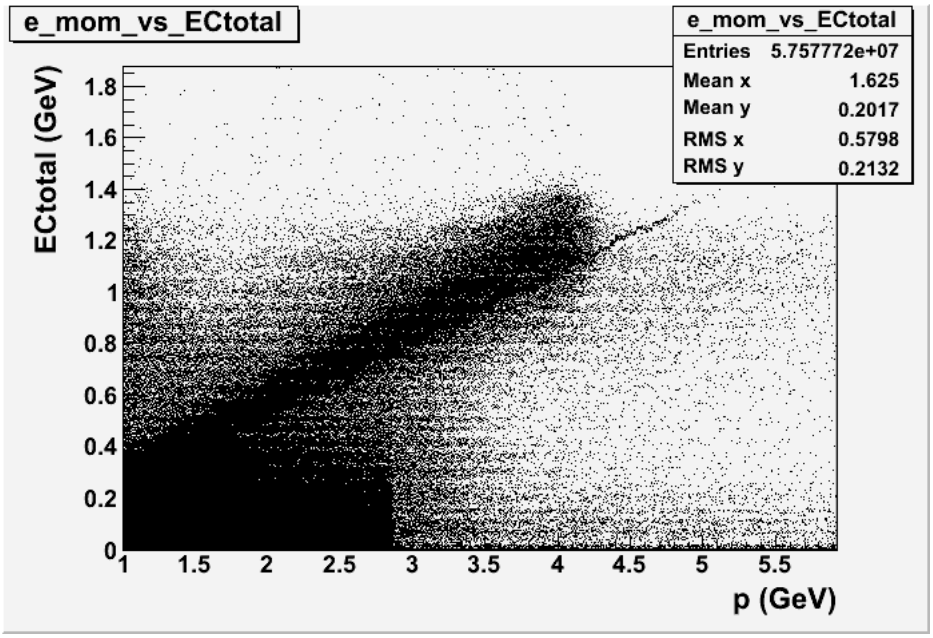

Fig. 1.2: Reconstructed electron momentum versus the electron energy deposited in the calorimeter (ECtotal).

the inner and outer calorimeter electron candidate's energy measured by the calorimeter and divided by the particle's momentum reconstructed by the drift chamber. As shown in Figure 1.3, there is an island near $E/p = 0.2$, which contains most of the electron candidates as well as some regions below 0.2 which will be argued to be negative pions misidentified as electrons.

Pions entering the calorimeter are typically minimum ionizing particles, loosing little of their incident energy in the calorimeter at a rate of 2 MeV $g^{-1}cm^2$. Electrons, on the other hand, deposit an amount of energy proportional to its momentum into the calorimeter. As a result, the energy deposited into the electromagnetic calorimeter is different for electrons and pions. Pions loose about 0.08 GeV of energy traversing the calorimeter independent their momentum thereby producing constant signal in the calorimeter around

0.08 GeV. In order to reduce misidentified pions from the electron sample, the following cut has been applied:

$$\mathrm{EC_{inner}} > 0.08 \times p, \tag{1.1}$$

where p represents a particle's momentum and $\mathrm{EC_{inner}}$ the energy deposited into the inner part of the calorimeter.

Since the energy loss of pions is related to the calorimeter thickness, a correlation can be established between the energy deposited into the inner and outer layers of the calorimeter:

$$\frac{\mathrm{EC_{tot}}}{\mathrm{EC_{inner}}} = \frac{13}{5}, \tag{1.2}$$

and results in the following cut for the energy deposition into the outer layer of the calorimeter:

$$\mathrm{EC_{tot}} > 0.2 \times p. \tag{1.3}$$

Cherenkov Counter Cut

The Cherenkov counter has been used to further reduce the negatively charged pion background in the reconstructed electron sample. When the velocity of a charged particle is greater than the local phase velocity of light or when it enters a medium with different optical properties, the charged particle can emit photons. Cherenkov light is emitted at the critical angle θ_c representing

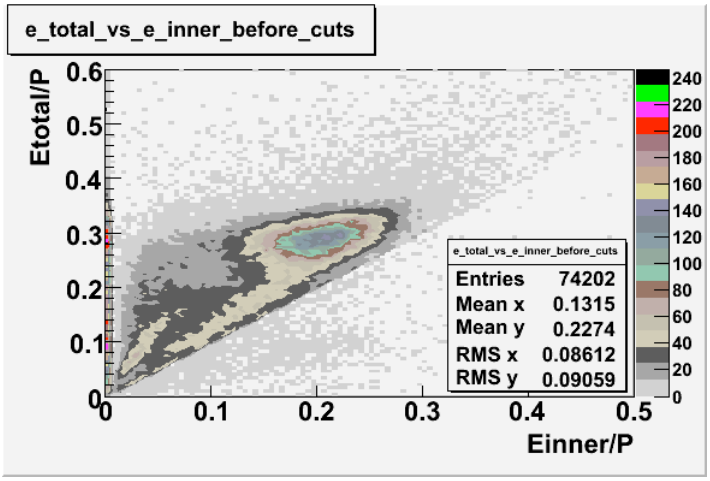

(a) Before cuts.

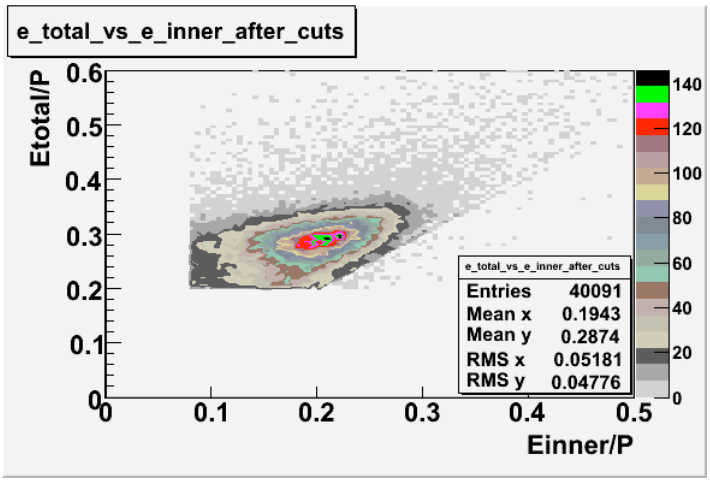

(b) After cuts.

Fig. 1.3: EC_{inner}/p versus EC_{tot}/p before and after EC cuts ($EC_{tot} > 0.2p$ and $EC_{inner} > 0.08p$). After applying EC cuts about 46% of the events have been removed from the electron sample.

the angle of Cherenkov radiation relative to the particle's direction. It can be shown that the cosine of the Cherenkov radiation angle is inversely proportional to the velocity of the charged particle

$$\cos\theta_c = \frac{1}{n\beta}, \tag{1.4}$$

where βc is the particle's velocity and n the index of refraction of the medium. The charged particle in time t travels a distance βct, while the electromagnetic waves travel $\frac{c}{n}t$. For a medium with given index of refraction n, there is a threshold velocity $\beta_{thr} = \frac{1}{n}$, below which no radiation is emitted. This process may be used to distinguish between the highly relativistic electrons and the less relativistic pions based on the number of photons produced in the Cherenkov detector. The number of photons produced per unit path length of a particle with charge Ze and per unit energy interval of the photons is proportional to the sine of the Cherenkov angle [3]

$$\frac{d^2N_{PE}}{dEdx} = \frac{\alpha z^2}{\hbar c}\sin^2\theta_c = \frac{\alpha z^2}{\hbar c}\left[1 - \frac{1}{\beta^2 n^2(E)}\right] \tag{1.5}$$

$$\frac{d^2N_{PE}}{d\lambda dx} = \frac{2\pi\alpha z^2}{\lambda^2}[1 - \frac{1}{\beta^2 n^2(\lambda)}] \tag{1.6}$$

$$\beta = \frac{v}{c} = \frac{pc}{\sqrt{(pc)^2 + (mc^2)^2}}. \tag{1.7}$$

Taylor expanding Eq. 1.6 and keeping only the first two terms we get following

$$\frac{d^2N_{PE}}{dEdx} = \frac{\alpha z^2}{\hbar c}\sin^2\theta_c = \frac{\alpha z^2}{\hbar c}[\beta^2 n^2(E) - 1]. \tag{1.8}$$

The gas used in the CLAS Cerenkov counter is perfluorobutane, C_4F_{10}, with an index of refraction equal to 1.00153. Approximately thirteen photo-electrons are produced by electrons traversing the Cherenkov detector. On the

other hand, calculations show that the number of photons produced by the negatively charged pions is approximately two. The theoretical results of the number of photons produced by electrons and pions when passing through the Cherenkov counter are shown on Figure 1.4.

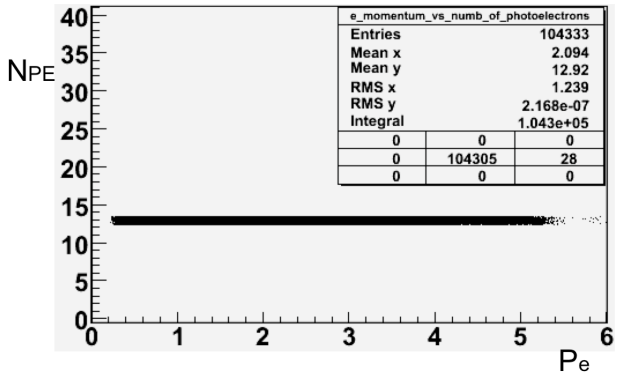

(a) For electrons.

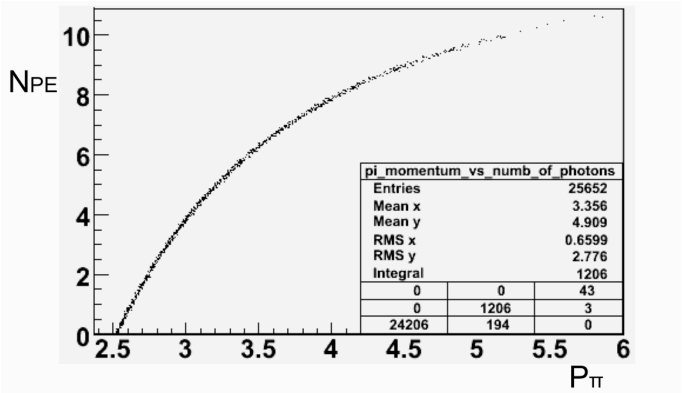

(b) For pions.

Fig. 1.4: Theoretical calculation of the number of photoelectrons for electrons and pions.

The distribution of the number of photoelectrons measured in the Cherenkov detector and the energy deposition dependence on number of photoelectrons are shown on Figure 1.5 and Figure 1.6, respectively. Pions, misidentified as electrons appear on Figure 1.5 at N_{PE}<2.5.

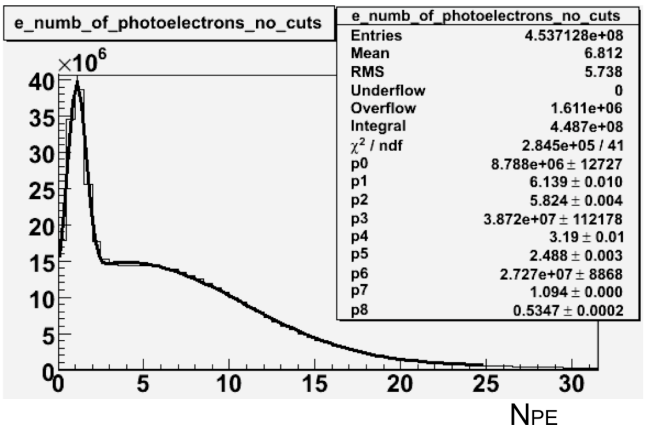

Fig. 1.5: The number of photoelectrons without cuts.

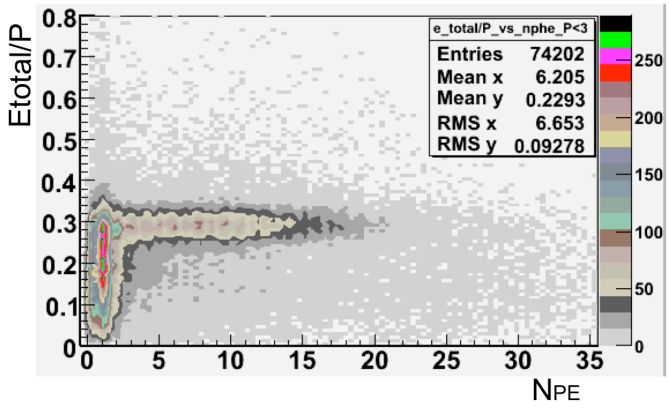

Fig. 1.6: The total energy deposited into the calorimeter versus the number of photoelectrons by the electron candidates.

Geometric and Timing Cuts

Negative pions may be misidentified as electrons when the electron scatters at a polar angle close to zero and is not observed by the detector. In order to reduce the electron sample contamination by those pions, geometrical cuts on the location of the particle at the entrance to the Cherenkov detector and time matching cuts have been developed by Osipenko [2]. For each CLAS Cherenkov detector segment, the following cut has been applied

$$|\theta_p - {\theta_p}^{\text{center}} - {\theta_p}^{\text{offset}}| < 3\sigma_p, \tag{1.9}$$

where θ_p represents the measured polar angle with respect to a projectile plane for each electron event and σ_p the width of the polar angle θ_p. The Cherenkov counter's projective plane is an imaginary plane behind the Cherenkov detector where Cherenkov radiation would have arrived if it had moved the same distance from the emission point to the PMT, without reflections in the mirror system. ${\theta_p}^{\text{center}}$ is the polar angle from the CLAS detector center to the image of Cherenkov counter segment center and ${\theta_p}^{\text{offset}}$ is the shift in the segment center position. In addition to geometrical cuts, timing cuts have been applied to match the time between a Cherenkov counter hit and the time of flight system.

The pion contamination in an electron sample was estimated by fitting the photoelectron distribution using two Gaussian distributions convoluted with a Landau distribution [4]:

$$N_{\text{PE}} = p_0 e^{-0.5\left(\frac{x-p_1}{p_2}\right)^2} + p4\frac{1}{1-\left(\frac{x-p5}{p6}\right)} + p_6 e^{-0.5\left(\frac{x-p_7}{p_8}\right)^2}. \tag{1.10}$$

The fits in Figure 1.7.(a) suggest that the pion contamination in the electron sample is $9.63\% \pm 0.01\%$ before applying the OSI cuts and after the OSI cuts the contamination is about $4.029\% \pm 0.003\%$ (Figure 1.7.(b)).

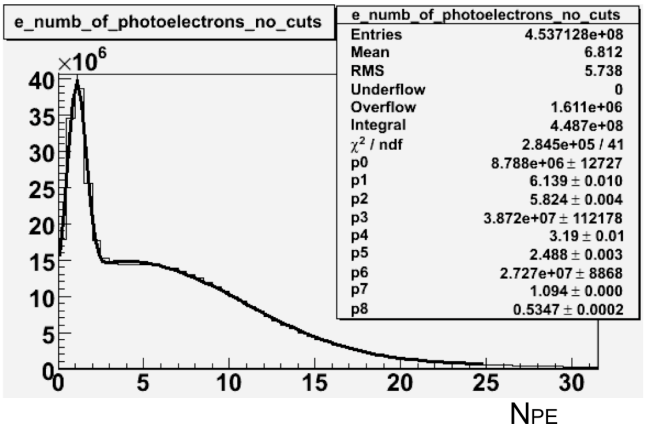

(a) Before Cuts.

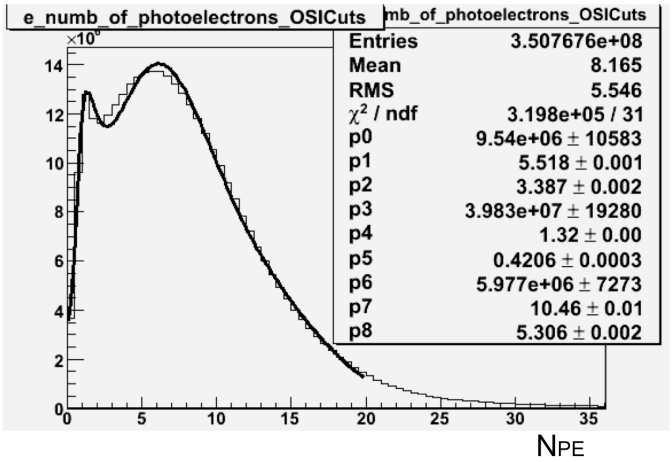

(b) After OSI Cuts.

Fig. 1.7: The number of photoelectrons generated by an electron candidate before and after geometrical and time matching cuts.

1.2.2 Pion Identification

Charged pions are identified using a coincidence hit in the drift chamber and Time-of-Flight (ToF) counter. Pions are separated from the other charged particles by looking at the particle's momentum versus its velocity (β). The particle velocity, $\beta = \frac{v}{c}$, is calculated from the difference of the RF time and the time-of-flight measurement in the ToF system with the path length from the

vertex to the ToF counters. The mass of the charged particle can be identified by combining the particle's β with the particle's momentum obtained from the track measured by the drift chamber in the known magnetic field. The particle's mass in a magnetic field is given as

$$p = \frac{m\beta}{\sqrt{1-\beta^2}} \tag{1.11}$$

$$m = p\sqrt{(\beta^2 - 1)} \tag{1.12}$$

$$\beta = \frac{L_{\text{path}}}{t_{\text{flight}}}, \tag{1.13}$$

where m is the mass of the charged particle, β its velocity, particle momentum p, L_{path} the path length from the vertex to scintillators, and t_{flight} the time of flight from the interaction vertex to the ToF system.

Using the above information (particle momentum from the drift chambers and the timing information from the ToF system), the mass squared of the charged particle was calculated and is shown on Figure 1.9. The pion mass band is distributed around zero. To isolate charged pions from the rest of the particles, a 3σ cut on the momentum versus β distribution has been applied [5].

In addition to the above 3σ cut, fiducial volume cuts have been applied to improve charged pion identification. For the EG1b experiment, pions were detected from 8° to 180° [5]. The pion identification code has been developed by Joshua Pierce [6].

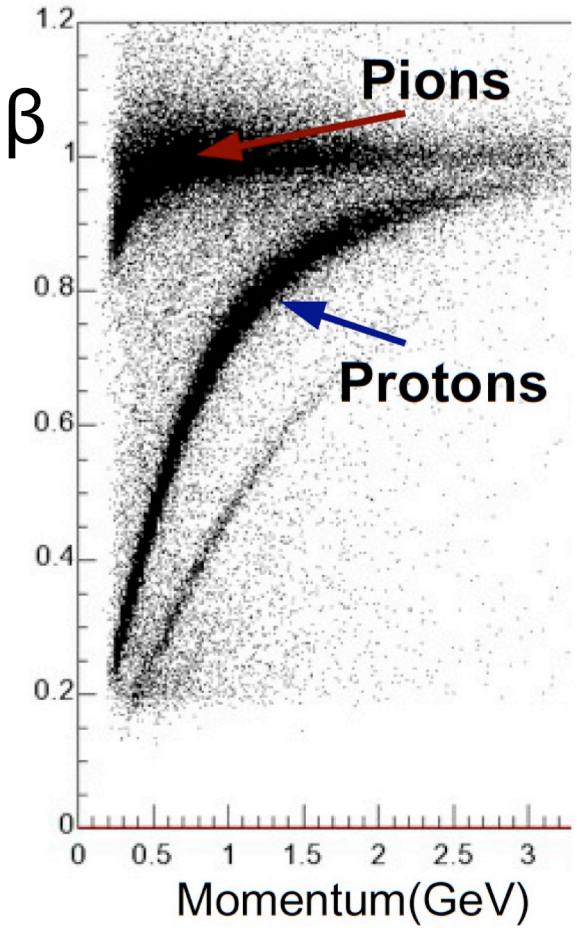

Fig. 1.8: The positively charged particle momentum versus β distribution. The pion and proton bands are clearly separated.

1.3 Event Reconstruction Efficiency

The goal of this work is to measure the semi-inclusive asymmetry when an electron and a pion are detected in the final state. For this analysis, pions of opposite charge will be observed using the same scintillator paddles by flipping the CLAS torus magnetic field direction. Although pions will be detected by the same detector elements, electrons will intersect different detector elements.

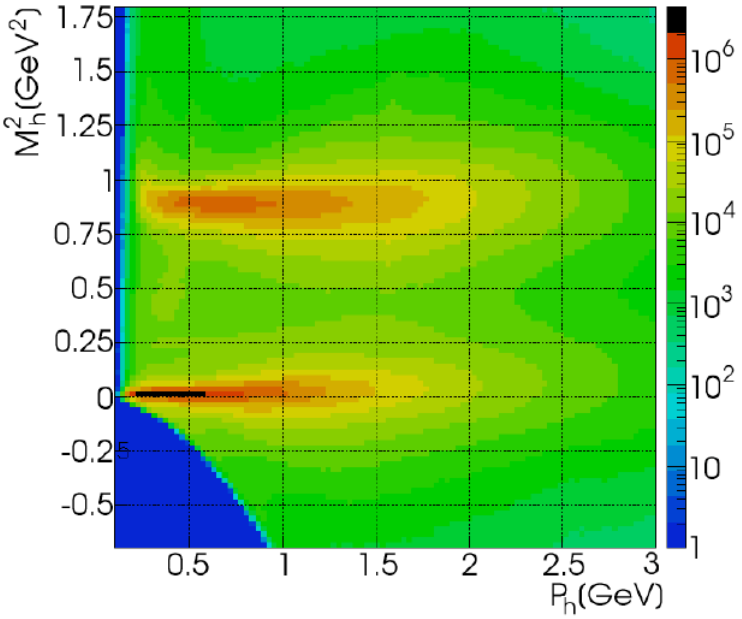

Fig. 1.9: The charged particle momentum versus mass squared distribution for the $\vec{e}p \rightarrow \vec{e}'\pi^+ n$ electroproduction process. The bands around zero and one represent pions and protons respectively [5].

As a result, the electron event reconstruction efficiency was evaluated in terms of the electron rate observed in two different scintillator paddles detecting the same electron kinematics.

1.3.1 Inclusive Electron Event Reconstruction Efficiency

The electron event reconstruction efficiency for individual scintillator detectors using the 4.2 GeV EG1b data set is investigated below. Only the electron is detected in the final state (inclusive case). The pion contamination in the electron sample was removed by applying the cuts described in section 1.2. The electron paddle numbers 10 (B<0) and 5 (B>0) were chosen respectively, because they contained the most electron events in a first pass semi-inclusive

pion analysis of the data set. The electron kinematics (momentum, scattering angle and invariant mass) for these scintillators is shown on Figure 1.10.

Ratios of the inclusive electron rate, normalized using the gated Faraday cup and detected in scintillator paddles # 5 and # 10, were measured. Two ratios are constructed to quantify the CLAS detector's ability to reconstruct electrons in scintillator paddle #5 using a positive torus polarity and scintillator #10 using a negative torus polarity.

$$\frac{\mathrm{ND_3, B} > 0, \text{Paddle Number}^{e^-} = 5}{\mathrm{ND_3, B} < 0, \text{Paddle Number}^{e^-} = 10} = 1.57 \pm 0.16 \tag{1.14}$$

$$\frac{\mathrm{NH_3, B} > 0, \text{Paddle Number}^{e^-} = 5}{\mathrm{NH_3, B} < 0, \text{Paddle Number}^{e^-} = 10} = 1.76 \pm 0.17. \tag{1.15}$$

The above ratios are statistically the same. The semi-inclusive analysis to be performed in this work will be taking ratios using an ND_3 and NH_3 target. Below is the observed ratio comparing the inclusive electrons in scintillator #5 for a positive torus polarity and an ND_3 target to the electrons in scintillator #10 when the torus polarity is negative and the target is NH_3.

$$\frac{\mathrm{ND_3, B} > 0, \text{Paddle Number}^{e^-} = 5}{\mathrm{NH_3, B} < 0, \text{Paddle Number}^{e^-} = 10} = 1.55 \pm 0.15. \tag{1.16}$$

The above ratios, which have been observed to be ammonia target independent, indicate a difference in an electron detector efficiency when the torus polarity is flipped. An electron detection efficiency "correction coefficient" is defined in terms of the above ratio and measured to be $\frac{\mathrm{ND_3, B>0, Paddle\ Number}^{e^-}=5}{\mathrm{NH_3, B<0, Paddle\ Number}^{e^-}=10} = 0.645$ and $\frac{\mathrm{ND_3, B<0, Paddle\ Number}^{e^-}=10}{\mathrm{NH_3, B>0, Paddle\ Number}^{e^-}=5} = 1.82$. The impact of these correc-

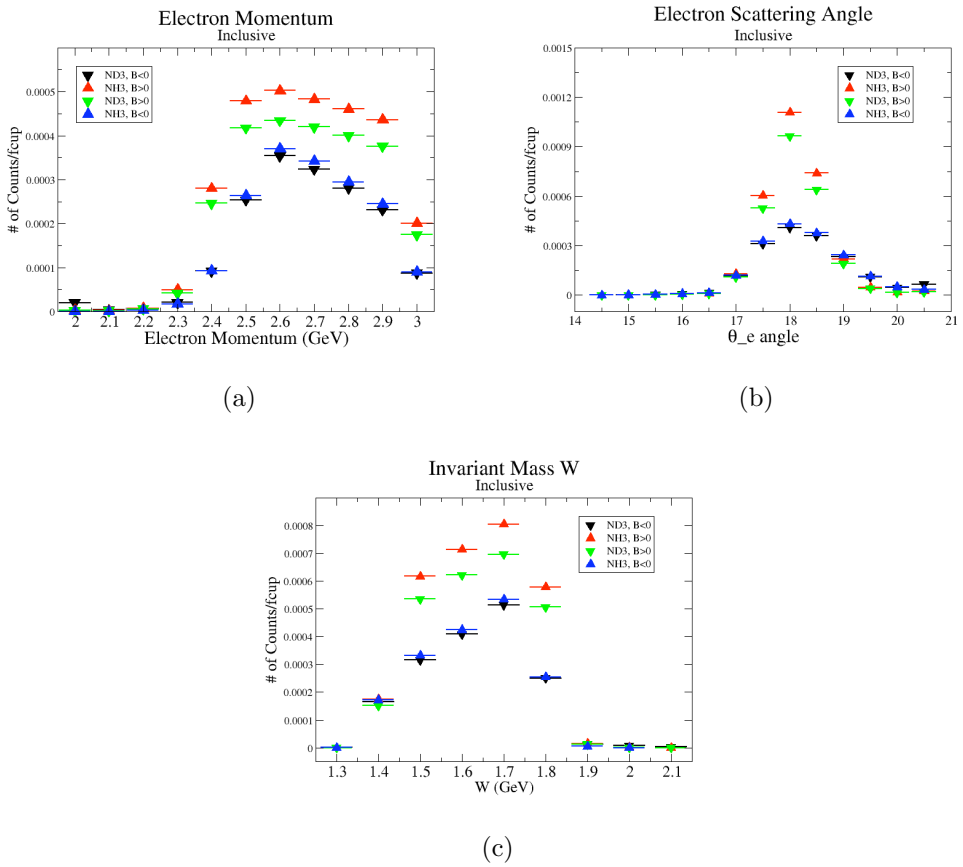

Fig. 1.10: Electron Kinematics. (a) Electron Momentum, (b) Electron Scattering Angle θ and (c) W Invariant mass((NH$_3$, B>0), (NH$_3$, B<0), (ND$_3$, B>0) and (ND$_3$, B<0))

tions on the data is illustrated in the next section.

1.3.2 Exclusive and Semi-Inclusive Event Reconstruction Efficiencies

The measured single pion electroproduction rate was compared to the MAID 2007 unitary model [7], that has been developed using the world data of pion photo and electro-production, to determine the impact of using the

above electron reconstruction efficiency "correction coefficient". The MAID 2007 model has predictions of the total cross section for the following two cases that are relevant to our work:

$$\gamma^* + \text{proton}(NH_3) \rightarrow \pi^+ + \text{neutron} \tag{1.17}$$

$$\gamma^* + \text{neutron}(ND_3) \rightarrow \pi^- + \text{proton}. \tag{1.18}$$

Using MAID 2007, the total cross section was calculated for the following invariant mass and four momentum transfer squared values: 1.7 GeV < W<1.8 GeV and Q^2=1.1 GeV^2 [7]. The exclusive total cross section for such reactions may be expressed as

$$\sigma = \sigma_T + \epsilon\sigma_L + \sqrt{2\epsilon(1+\epsilon)}\sigma_{LT}\cos\phi_\pi{}^{CM} + \epsilon\sigma TT\cos 2\phi_\pi{}^{CM} + \\ + h\sqrt{2\epsilon(1-\epsilon)}\sigma_{LT'}\sin\phi_\pi{}^{CM}, \tag{1.19}$$

where $\phi_\pi{}^{CM}$ is the pion azimuthal angle in the CM frame, $\epsilon = (1 + 2(1 + \frac{\nu^2}{Q^2})\tan^2\frac{\theta_e}{2})^{-1}$ is the virtual photon polarization, $\nu = E_i - E_f$ the energy difference of the initial and final state electron, $Q^2 = 4E_iE_f\sin^2\frac{\theta_e}{2}$ the four momentum transfer squared, θ_e the electron scattering angle and h the electron helicity.

The ratio of the pions detected for the opposite torus particles in the scintillator paddles, located between the Cherenkov counter and electromagnetic calorimeter, is shown in Figure 1.11. Ratios were measured for four different cases. The intrinsic assumption is that, for the inbending case, positive

pions and for the outbending case negative pions have the same trajectories when they have the same kinematics. In addition, negatively charged pions in the inbending field and positively charged pions in the outbending fields are detected by the same detector elements.

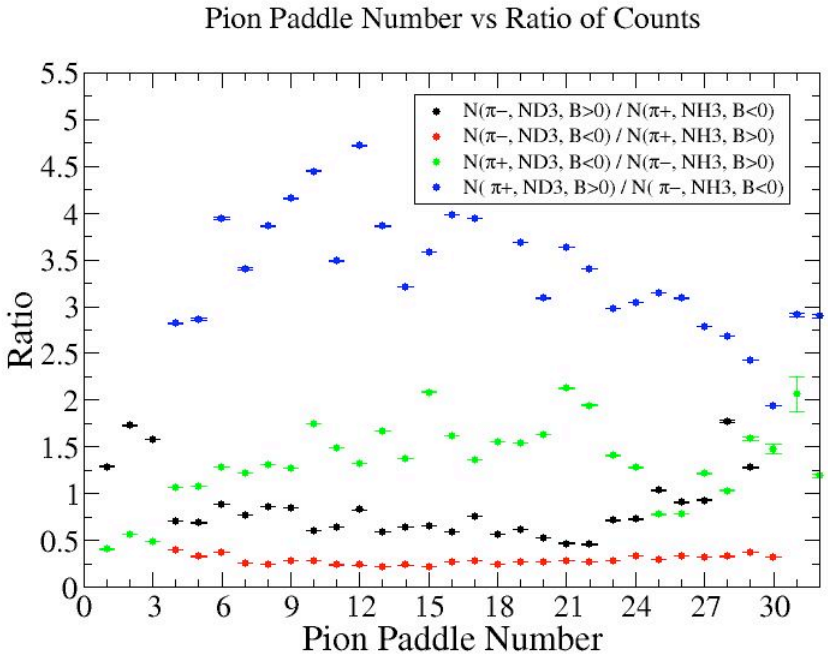

Fig. 1.11: Pion paddle number versus the Semi-Inclusive ratio.

After applying corrections determined by the inclusive events, the ratios were compared to the results from MAID2007. The difference of the measured and MAID2007 model ratios for each pion paddle number is shown in Figure 1.12. One can argue, using Figure 1.12, that the ”inclusive corrections” do not impact single pion production rates for the exclusive cases.

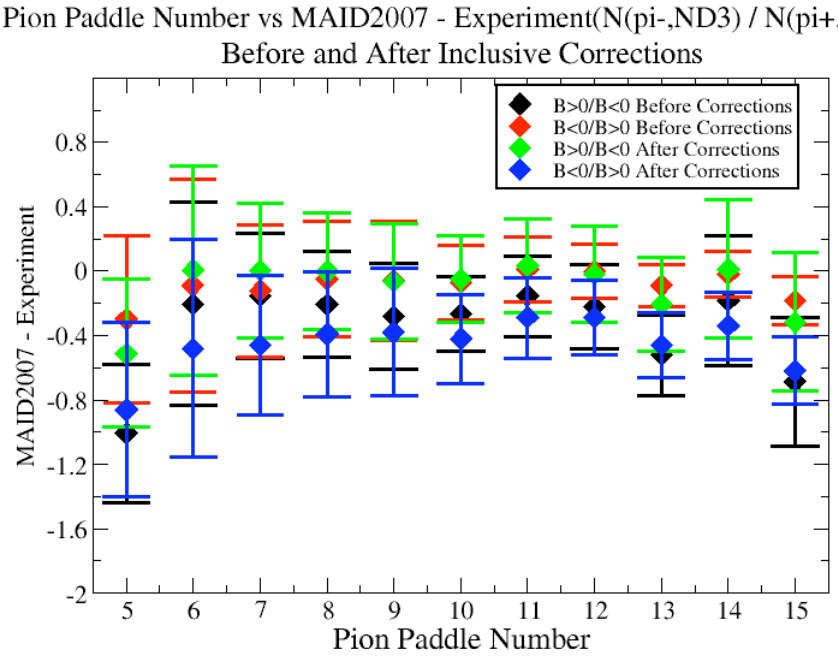

Fig. 1.12: Pion Paddle Number versus MAID2007 - Experiment(N (π^-, ND_3) / N(π^+, NH_3)). The Black and red data represent B>0/B<0 and B<0/B>0 cases respectively before corrections. The green and blue points represent the ratios for B>0/B<0 and B<0/B>0 after inclusive corrections.

1.4 Asymmetries

The double spin asymmetry measurements in this work are performed by comparing scattering events that occur when the incident probe spin and nuclear target spin are parallel to the scattering events that occur when the spins are anti-parallel.

1.4.1 Beam Charge Asymmetry

The helicity of the electron beam was flipped at a rate of 1 Hz. The helicity is prepared at the source such that helicity pairs are produced pseudo randomly.

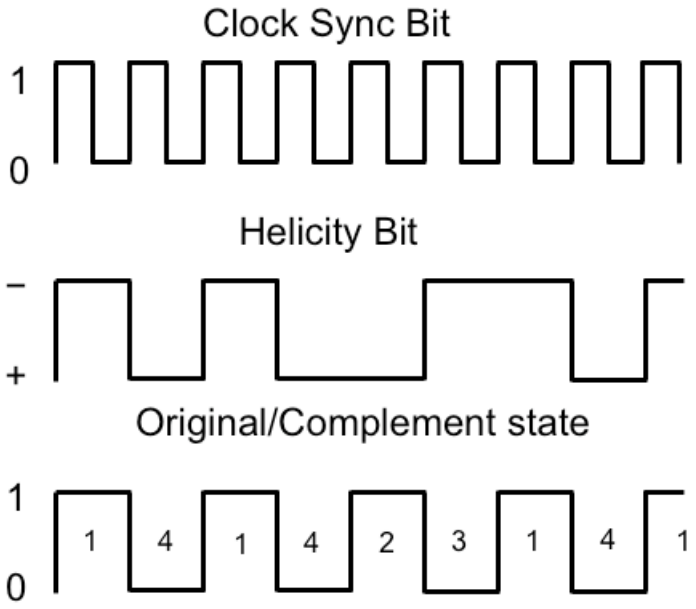

Fig. 1.13: The Helicity State: A one bit signal from the beam injector gives the helicity information. A sync bit with a 2 Hz frequency is generated to indicate the start of a helicity state.

If the first electron bunch is pseudo randomly chosen to be positive (negative) then it is labeled as the original helicity state and denoted in software by a 2 (1). The next helicity state is prepared to be a complement to the first state and labeled in the software as either a 4, if the original helicity state was a 1 (negative), or 3 if the original helicity state was a 2 (positive). The helicity selection process is then repeated.

Figure 1.13 illustrates the signals used to label the helicity states. The

clock pulse (SYNC) is used to indicate that a change in the pockel cell used to define the helicity state may have occurred. The helicity bit identifies the helicity state that was set. The original/complement pulse identifies if the state is an original or complement helicity state. All three bits are recorded in the raw data file for each event and then converted to the labels 1, 2, 3, 4 during data summary tape (DST) production once the particles have been reconstructed.

Two scalers were used to record several ancillary detectors, such as a Faraday cup and several PMTs mounted on the beam line, according to their helicity label. One of the scalers was gated by the data acquisition (DAQ) live time in order to record beam conditions when the DAQ was able to take data and not busy recording data. The second scaler remained ungated. Both scalers recorded the SYNC and Helicity signals from the injector along with the counts observed from ancillary detectors during the SYNC interval. The Faraday cup signal recorded by the gated helicity scaler is used to normalize the events reconstructed during the same helicity interval.

The beam charge asymmetry is defined in Eq. 1.20 and measured using the gated helicity scaler. For each run number, a gaussian fit was used to fit the beam charge asymmetry distributions as in Figure 1.14. The beam charge asymmetry is defined as

$$A_{14} = \frac{\Sigma FC_i^{\text{hel1}} - \Sigma FC_i^{\text{hel4}}}{\Sigma FC_i^{\text{hel1}} + \Sigma FC_i^{\text{hel4}}}, \tag{1.20}$$

$$A_{23} = \frac{\Sigma FC_i^{\text{hel2}} - \Sigma FC_i^{\text{hel3}}}{\Sigma FC_i^{\text{hel2}} + \Sigma FC_i^{\text{hel3}}}, \tag{1.21}$$

where $FC^{\text{hel1,hel2}}$ ($FC^{\text{hel4,hel3}}$) represents the Faraday cup counts observed

for the original helicity 1 and 2 states (the complement helicity 3 and 4 states).

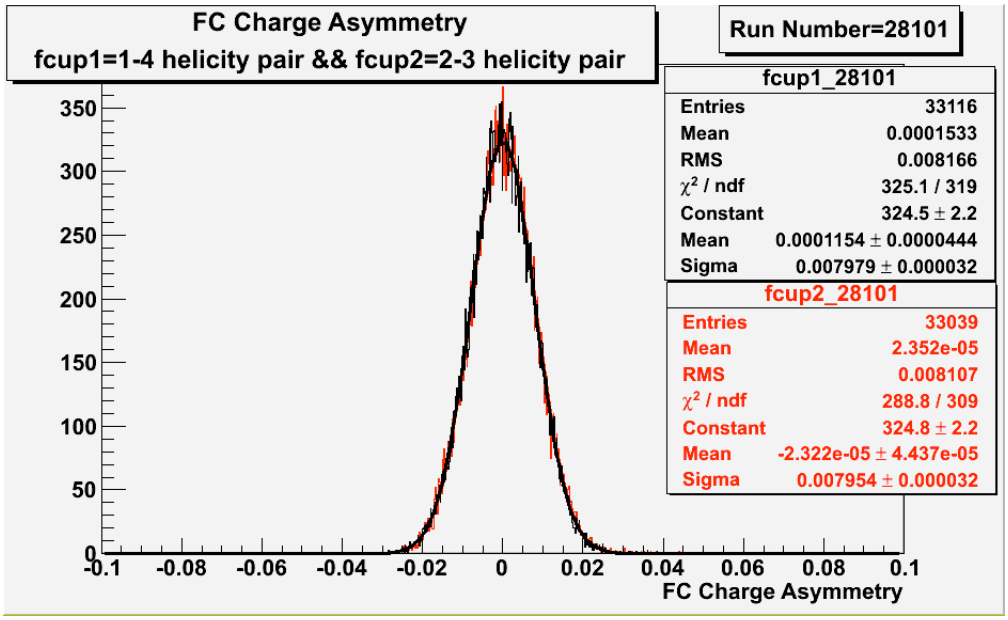

Fig. 1.14: Beam charge asymmetry for run #28101 using the gated Faraday cup counts for two helicity pairs (1-4 and 2-3 helicity pairs). $A_{1-4} = (11.5 \pm 4.4) \times 10^{-5}$ and $A_{2-3} = (-2.3 \pm 4.4) \times 10^{-5}$.

EG1b data sets, with the same half wave plate, target type, target polarization, and beam torus have been combined. The beam charge asymmetries have been calculated for the each run group and are listed in Table 1.2.

Run Group	Half wave plate(HWP)	$A_{1-4} \times 10^{-4}$	$A_{2-3} \times 10^{-4}$
28100 – 28105	+1	5.88 ± 34.40	4.03 ± 34.36
28106 – 28115	-1	7.53 ± 22.30	8.28 ± 22.30
28145 – 28240	+1	31.70 ± 7.99	30.40 ± 7.99
28242 – 28284	-1	49.6 ± 10.8	47.9 ± 10.8
28286 – 28324	+1	36.3 ± 11.6	37.0 ± 11.5
28325 – 28447	-1	21.1 ± 13.4	22.2 ± 13.4
28449 – 28479	+1	-11.6 ± 16.5	-21.6 ± 16.5

Table 1.2: Run Group versus Beam Charge Asymmetry.

1.4.2 Electron Asymmetry

A measurement of the electron cross section helicity difference needs to account for a possible helicity dependence of the incident electron flux (charge asymmetry). Figure 1.15 shows the reconstructed electron rate asymmetry, before it is normalized by the gated Faraday Cup, as a function of the run number for the 4.2 GeV data set. The reconstructed electron asymmetry can be defined following way:

$$A_{NES}^{+-} = \frac{\Sigma NES^{+} - \Sigma NES^{-}}{\Sigma NES^{+} + \Sigma NES^{-}} = \frac{\Sigma NES^{\mathrm{hel2}} - \Sigma NES^{\mathrm{hel3}}}{\Sigma NES^{\mathrm{hel2}} + \Sigma NES^{\mathrm{hel3}}} \equiv (2-3), \quad (1.22)$$

or

$$A_{NES}^{-+} = \frac{\Sigma NES^{-} - \Sigma NES^{+}}{\Sigma NES^{-} + \Sigma NES^{+}} = \frac{\Sigma NES^{\mathrm{hel1}} - \Sigma NES^{\mathrm{hel4}}}{\Sigma NES^{\mathrm{hel1}} + \Sigma NES^{\mathrm{hel4}}} \equiv (1-4), \quad (1.23)$$

where NES^{+} (NES^{-}) represents number of electron scattered for the positive (negative) beam helicity state.

Systematic effects on the asymmetry measurement may be investigated by separating the data into two groups based on which helicity state is set first. The first group (black data points) represents the electron asymmetry observed when the first (original) helicity state is negative and its complement state is positive (helicity state #1 – state #4). The second group (red data points) represents the asymmetry observed when the first state is positive and the complement state is negative (helicity state #2 – #3). Both groups were divided into two subgroups based the target type used. The diamond points

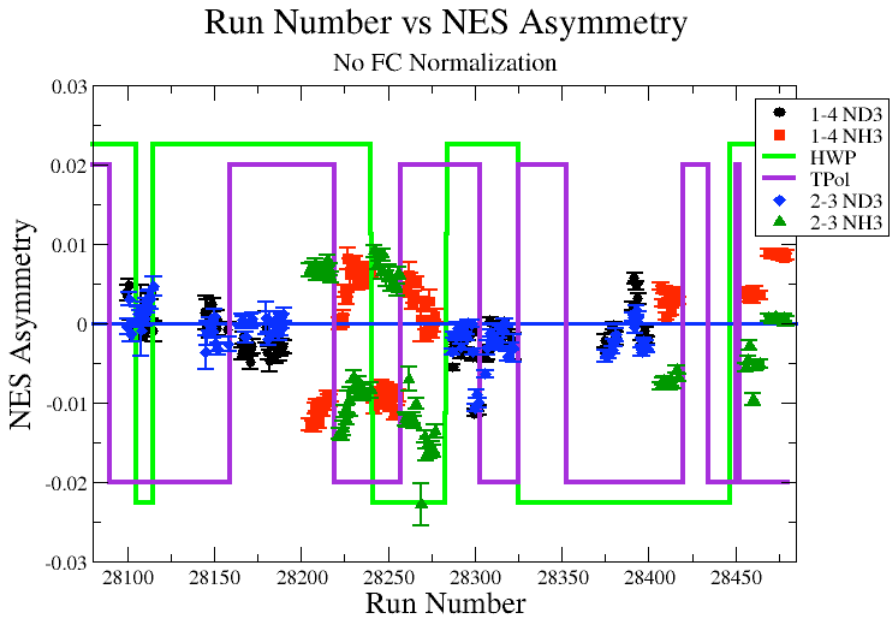

Fig. 1.15: Run Number versus Electron Asymmetry before FC normalization. The black and red points represent reconstructed electron asymmetry for the helicity 1-4 pair for ND_3 and NH_3 target respectively. The blue and green points represent the helicity pair 2-3 for ND_3 and NH_3 respectively. The green line shows the sign of the half wave plate (HWP) and the purple line is the sign of the target polarization (TPol).

on the histogram represent the data for the NH_3 target and the squares for the ND_3 target. Two lines on the histogram are used to identify the sign of the half wave plate (HWP) and the target polarization (TPol). The relative spin orientation can be changed by either inserting a half wave plate (HWP) or by populating a different target polarization state with a different RF frequency. One would expect the asymmetry to change sign if either the HWP is inserted or the target polarization is rotated 180 degrees. As one can see for Figure 1.15 and Figure 1.16, the electron asymmetry changes sign if the HWP or the target polarization is reversed.

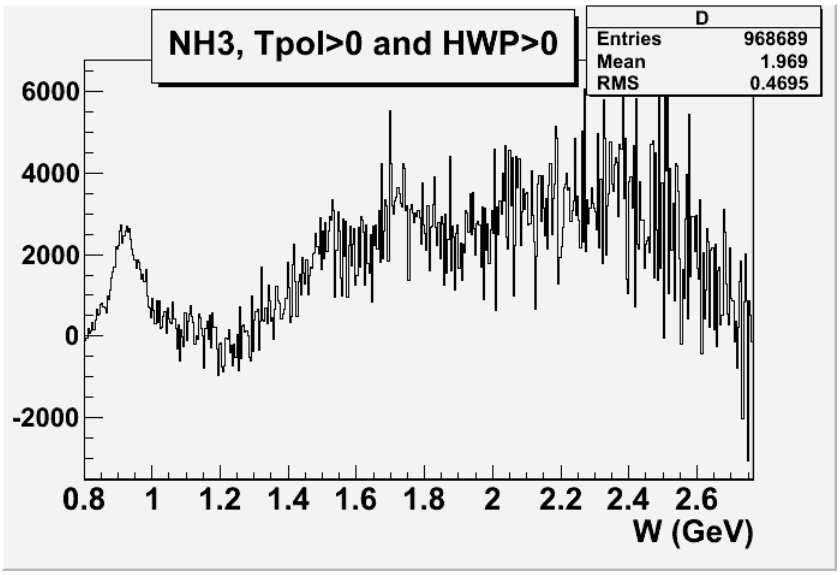

(a) NH3, Tpol>0 and HWP>0.

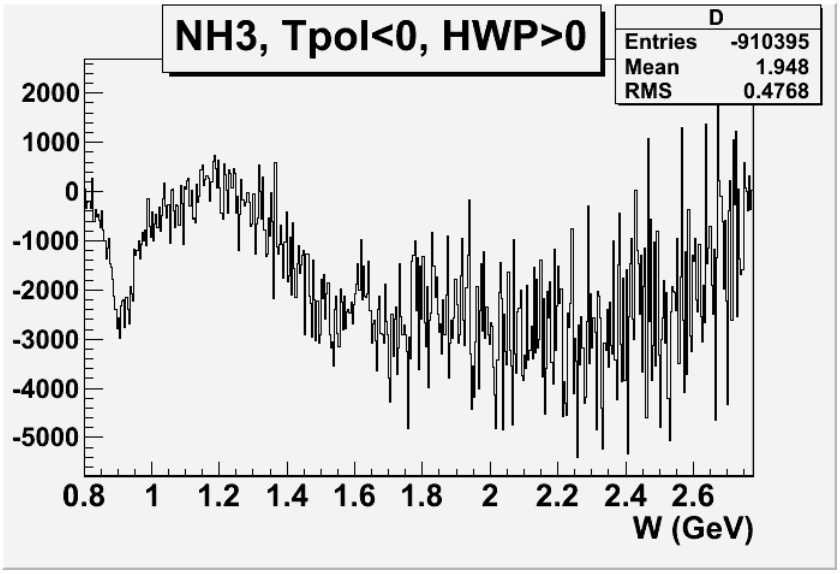

(b) NH3, Tpol<0 and HWP>0.

Fig. 1.16: W versus ($NES^{\mathrm{hel4}} - NES^{\mathrm{hel1}}$) and ($NES^{\mathrm{hel2}} - NES^{\mathrm{hel3}}$). The electron asymmetry changes sign when the target polarization is reversed.

The un-normalized reconstructed electron asymmetry has been calculated as:

$$A_{NES}^{-+} = \frac{\Sigma NES^{\text{hel1}} - \Sigma NES^{\text{hel4}}}{\Sigma NES^{\text{hel1}} + NES^{\text{hel4}}}, \tag{1.24}$$

$$A_{NES}^{+-} = \frac{\Sigma NES^{\text{hel2}} - \Sigma NES^{\text{hel3}}}{\Sigma NES^{\text{hel2}} + NES^{\text{hel3}}}, \tag{1.25}$$

and the Faraday cup normalized as

$$A_{\text{NES}}^{+-} = \frac{\frac{\Sigma NES^{\text{hel2}}}{\Sigma FC^{\text{hel2}}} - \frac{\Sigma NES^{\text{hel3}}}{\Sigma FC^{\text{hel3}}}}{\frac{\Sigma NES^{\text{hel2}}}{\Sigma FC^{\text{hel2}}} + \frac{\Sigma NES^{\text{hel3}}}{\Sigma FC^{\text{hel3}}}}. \tag{1.26}$$

1.4.3 Semi-Inclusive Asymmetries

The asymmetries from semi-inclusive pion electroproduction using proton or deuteron targets can be written in terms of the difference of the yield when the electron spin is parallel and antiparallel to the spin of the nucleon. There are four combinations of semi-inclusive asymmetries: $A_{\text{NH}_3}^{\pi^+}$, $A_{\text{NH}_3}^{\pi^-}$, $A_{\text{ND}_3}^{\pi^+}$ and $A_{\text{ND}_3}^{\pi^-}$

$$A_{\text{NH}_3}^{\pi^+} \equiv \frac{\Sigma N_{\text{NH}_3,\pi^+}^{\uparrow\uparrow} - \Sigma N_{\text{NH}_3,\pi^+}^{\uparrow\downarrow}}{\Sigma N_{\text{NH}_3,\pi^+}^{\uparrow\uparrow} + \Sigma N_{\text{NH}_3,\pi^+}^{\uparrow\downarrow}} \tag{1.27}$$

$$A_{\text{NH}_3}^{\pi^-} \equiv \frac{\Sigma N_{\text{NH}_3,\pi^-}^{\uparrow\uparrow} - \Sigma N_{\text{NH}_3,\pi^-}^{\uparrow\downarrow}}{\Sigma N_{\text{NH}_3,\pi^-}^{\uparrow\uparrow} + \Sigma N_{\text{NH}_3,\pi^-}^{\uparrow\downarrow}} \tag{1.28}$$

$$A_{\text{ND}_3}^{\pi^+} \equiv \frac{\Sigma N_{\text{ND}_3,\pi^+}^{\uparrow\uparrow} - \Sigma N_{\text{ND}_3,\pi^+}^{\uparrow\downarrow}}{\Sigma N_{\text{ND}_3,\pi^+}^{\uparrow\uparrow} + \Sigma N_{\text{ND}_3,\pi^+}^{\uparrow\downarrow}} \tag{1.29}$$

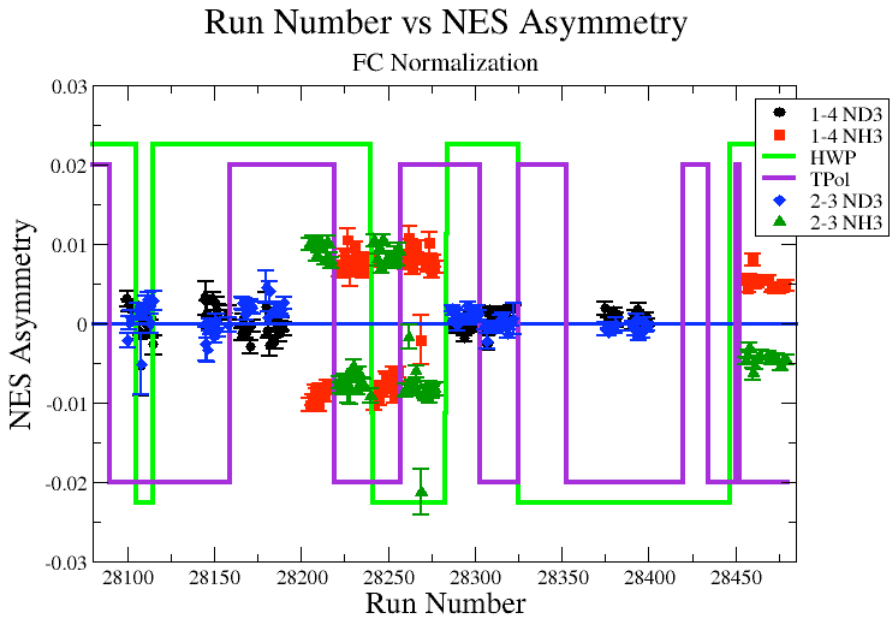

Fig. 1.17: Run number versus electron asymmetry after applying FC normalization. The black and red points represent the reconstructed electron asymmetry for the helicity 1-4 pair for ND_3 and NH_3 target respectively. The blue and green points are the helicity pair 2-3 for ND_3 and NH_3 respectively. The green line shows the sign of the half wave plate (HWP) and the purple line is the sign of the target polarization (TPol).

$$A^{\pi^-}_{\mathrm{ND}_3} \equiv \frac{\Sigma N^{\uparrow\uparrow}_{\mathrm{ND}_3,\pi^-} - \Sigma N^{\uparrow\downarrow}_{\mathrm{ND}_3,\pi^-}}{\Sigma N^{\uparrow\uparrow}_{\mathrm{ND}_3,\pi^-} + \Sigma N^{\uparrow\downarrow}_{\mathrm{ND}_3,\pi^-}}, \tag{1.30}$$

where $N^{\uparrow\downarrow}_{\mathrm{NH}_3,\pi^+,\pi^-}(N^{\uparrow\uparrow}_{\mathrm{NH}_3,\pi^+,\pi^-})$ and $N^{\uparrow\downarrow}_{\mathrm{ND}_3,\pi^+,\pi^-}(N^{\uparrow\uparrow}_{\mathrm{ND}_3,\pi^+,\pi^-})$ represent the number of π^+ and π^- hadrons detected in the final state with the scattered electron when the spin of the initial electron beam was antiparallel (parallel) to the spin of the proton and neutron respectively.

The kinematic coverage for the events used in the measured asymmetries

are shown on Figure 1.18 and Figure 1.19. The semi-inclusive asymmetries are listed in Table 1.3. The first group $A_{\text{hel1-hel4}}$ represents the asymmetry measured when the first original electron spin (hel1) is antiparallel to the target nucleon spin and its complement state (hel4) is parallel, whereas the second group $A_{\text{hel2-hel3}}$ represents measuring the SIDIS asymmetry when the first helicity state is parallel (hel2) and its complement state (hel3) is antiparallel to the spin of the nucleon. For the final measurement, the two groups are combined into one $A_{\text{hel42-hel13}}$ set, in order to increase statistics. Instead of looking at original and complement electron helicity states, they have been combined into the positive (hel42) and negative (hel13) helicity states, which are parallel and antiparallel to the spin of the target nucleon respectively.

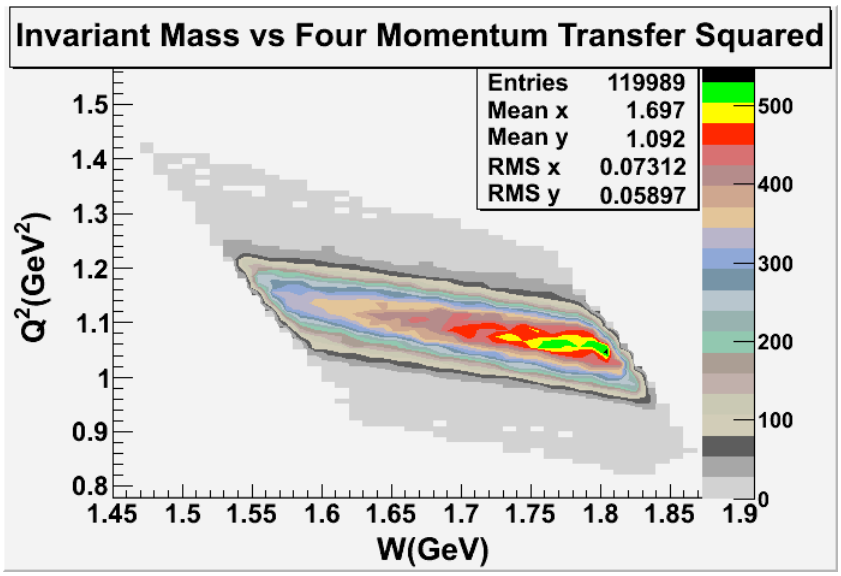

Fig. 1.18: Invariant Mass versus Q^2.

The ratio of the combined semi-inclusive deep inelastic asymmetries (A^{raw}) from Table 1.3, for two different torus settings have been corrected for the electron event reconstruction efficiency. Figure 1.20 represents the raw

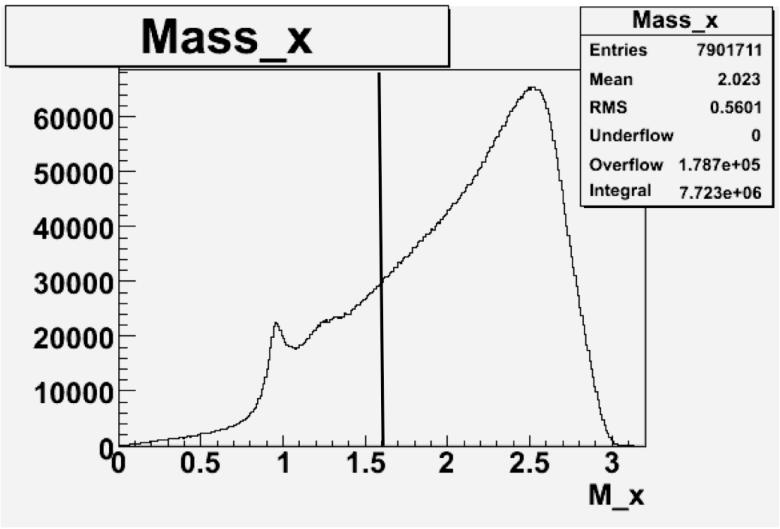

Fig. 1.19: Missing Mass. The vertical line represents the semi-inclusive cut which removes events with M_x<1.6 GeV^2.

Target type, Beam Torus	$A_{\text{hel1-hel4}} \times 10^{-4}$	$A_{\text{hel2-hel3}} \times 10^{-4}$	$A^{\text{raw}} \times 10^{-4}$
NH_3, B>0, π^+	-139.84 ± 81.52	143.15 ± 81.78	136.2 ± 57.74
NH_3, B<0, π^+	-223.76 ± 117.10	247.65 ± 116.59	237.69 ± 82.65
ND_3, B>0, π^-	-6.37 ± 188.73	-98.11 ± 188.03	9.21 ± 127.22
ND_3, B<0, π^-	-63.73 ± 105.14	-30.34 ± 6085.54	12.37 ± 71.10
NH_3, B>0, π^-	-155.45 ± 128.21	-72.55 ± 128.92	35.11 ± 90.91
NH_3, B<0, π^-	9.60 ± 119.31	72.94 ± 119.36	32.39 ± 84.38
ND_3, B>0, π^+	-76.59 ± 126.60	110.28 ± 126.13	92.25 ± 85.38
ND_3, B<0, π^+	-29.22 ± 107.53	123.98 ± 106.86	92.25 ± 85.38

Table 1.3: SIDIS asymmetry for each type target material and beam torus.

asymmetry ratios before and after electron event reconstruction efficiency corrections. The ratios have been calculated for each target and charged pion type. The SIDIS asymmetries before and after the correction are statistically the same. The result indicates that the electron event reconstruction efficiency does not change the asymmetries.

The data have been combined for each target type and asymmetries mea-

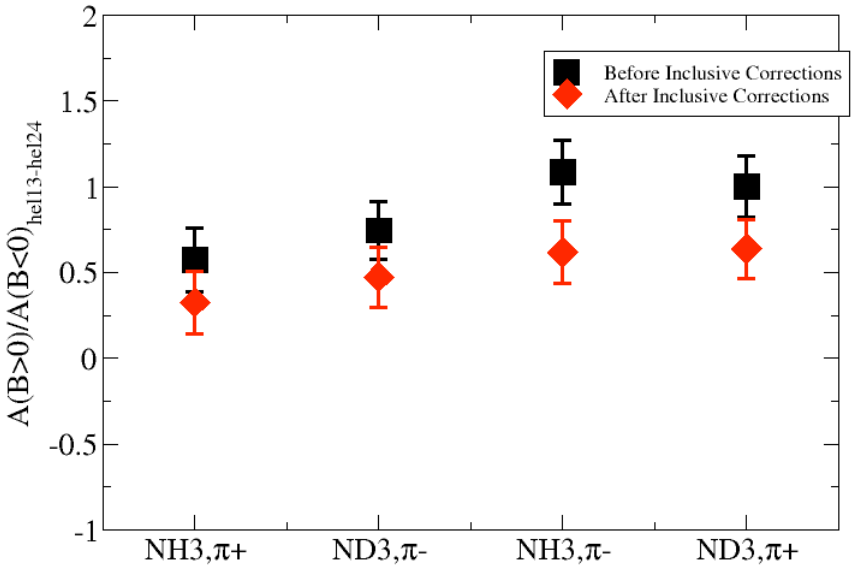

Fig. 1.20: The ratio of the SIDIS asymmetries for two torus field settings $\frac{A^{raw}(\mathrm{B}>0)}{A^{raw}(\mathrm{B}<0)}$ versus target and the charged pion type. The black squares represent the data before electron reconstruction efficiency and the red data - after electron reconstruction efficiency has been applied.

sured for two x_B values (Table 1.4). The SIDIS asymmetries were calculated for the following kinematic range: electron scattering angle $17.5<\theta_e<18.5$, electron momentum 2.55 GeV$<$ P$_e$$<$2.75 GeV, invariant mass 1.6 GeV$<$W$<$1.8 GeV, missing mass M$_x$$>$1.6 GeV^2 and momentum transfer squared 0.9 GeV^2$<$Q^2$<$1.3 GeV^2.

In addition to x_B, the data have been subdivided according to the fractional energy of the observed final state pion(z = 0.4 and z = 0.7). $A_{\mathrm{NH_3}}^{\pi^+,\mathrm{raw}}$ asymmetries for two z are shown in Table 1.5.

SIDIS Asymmetry	$x_B = 0.3$	$x_B = 0.4$
$A_{NH_3}^{\pi^+,raw}$	$(150.08 \pm 65.96) \times 10^{-4}$	$(217.20 \pm 69.06) \times 10^{-4}$
$A_{ND_3}^{\pi^-,raw}$	$(39.04 \pm 81.44) \times 10^{-4}$	$(91.90 \pm 96.14) \times 10^{-4}$
$A_{NH_3}^{\pi^-,raw}$	$(100.81 \pm 83.49) \times 10^{-4}$	$(-23.98 \pm 94.92) \times 10^{-4}$
$A_{ND_3}^{\pi^+,raw}$	$(53.17 \pm 74.89) \times 10^{-4}$	$(85.17 \pm 82.97) \times 10^{-4}$

Table 1.4: SIDIS asymmetries for $x_B = 0.3$ and $x_B = 0.4$.

z	$x_B = 0.3$	$x_B = 0.4$
0.4	$(125.62 \pm 81.92) \times 10^{-4}$	$(165.81 \pm 86.76) \times 10^{-4}$
0.7	$(140.32 \pm 158.98) \times 10^{-4}$	$(238.34 \pm 156.79) \times 10^{-4}$

Table 1.5: $A_{NH_3}^{\pi^+,raw}$ SIDIS asymmetry.

1.4.4 Dilution Factor

To account for the contributions of polarized nucleons from the nitrogen nuclei in the ammonia target and the cooling material of the target (Helium) cell to the semi-inclusive rates, the measured raw double spin asymmetries have to be divided by a dilution factor. The dilution factor accounts for the fraction of events coming from the desired polarized target nucleon. The dilution factors are calculated by combining the data from runs using different target types. During the EG1b experiment, several runs were taken with Carbon (C^{12}) and an empty target cell (Helium). All the runs in this work used liquid Helium as the coolant during the experiment. The Carbon and empty target runs were used to estimate the dilution of the data by the background attributed to the interaction of the incident electron beam with the Nitrogen or Helium nucleons present in the target cell [8].

In order to calculate the dilution factor, we need to define the number

of counts with beam helicity negative and positive for ammonia ($N_{\rm A}$), Carbon ($N_{\rm C}$) and empty target ($N_{\rm MT}$) runs. All are weighted by the corresponding gated Faraday Cup counts [9]. Normalized rates for Carbon and empty target types are defined as

$$n_{\rm C,MT} = \frac{N^{+}_{\rm C,MT} + N^{-}_{\rm C,MT}}{FC^{+} + FC^{-}} \tag{1.31}$$

and

$$n_{\rm A} = \frac{1}{2}(\frac{N^{+}_{\rm A}}{FC^{+}} + \frac{N^{-}_{\rm A}}{FC^{-}}), \tag{1.32}$$

where $n_{\rm C}$ is the rate from a Carbon target, $n_{\rm MT}$ is from an empty target and $n_{\rm A}$ is from one of the NH_3 or ND_3 ammonia targets.

The counts for all four targets (empty, Carbon and ammonia) can be expressed as the sum of counts from the entrance and exit window foils ($\rho_{\rm F}$, $l_{\rm F}$, $\sigma_{\rm F}$), liquid Helium coolant ($\rho_{\rm He}$, $l_{\rm He}$, $\sigma_{\rm He}$), Carbon($\rho_{\rm C}$, $l_{\rm C}$, $\sigma_{\rm C}$), Nitrogen ($\rho_{\rm N}$, $l_{\rm N}$, $\sigma_{\rm N}$), Hydrogen (Deuterium) ($\rho_{\rm H(D)}$, $l_{\rm H(D)}$, $\sigma_{\rm H(D)}$).

$$n_{\rm MT} = \rho_{\rm F} l_{\rm F} \sigma_{\rm F} + \rho_{\rm He} L \sigma_{\rm He} = f \rho_{\rm C} l_{\rm C} \sigma_{\rm C} + \rho_{\rm He} L \sigma_{\rm He}, \tag{1.33}$$

$$n_{\rm C} = \rho_{\rm F} l_{\rm F} \sigma_{\rm F} + \rho_{\rm C} l_{\rm C} \sigma_{\rm C} + \rho_{\rm He} (L - l_{\rm C}) \sigma_{\rm He}, \tag{1.34}$$

and

$$n_{\rm A} = \rho_{\rm F} l_{\rm F} \sigma_{\rm F} + \rho{\rm He} (L - l_{\rm A}) \sigma_{\rm He} + \rho_{\rm A} l_{\rm A} (\sigma_{\rm N} + 3\sigma_{\rm H(D)}), \tag{1.35}$$

where $f \equiv \frac{\rho_{\rm F} l_{\rm F} \sigma_{\rm F}}{\rho_{\rm C} l_{\rm C} \sigma_{\rm C}}$, $\sigma_{\rm H(D)}$ represents the Hydrogen (Deuteron) cross section.

Using the above system of equations, we define two new spectra to account for the Carbon target and the difference in the amount of Helium in ammonia targets versus the Carbon target. For a target cell with length L and the Carbon target with length $l_{\rm C}$, the Carbon and liquid He (LHe) contributions can be written following way:

$$n'_{\rm 12C} = \frac{L}{L + f l_{\rm C}} n_{\rm C} - \frac{L - l_{\rm C}}{L + f l_{\rm C}} n_{\rm MT} = \rho_{\rm C} l_{\rm C} \sigma_{\rm C} \tag{1.36}$$

and

$$n'_{\rm 4He} = \frac{(1+f) l_{\rm He}}{L + f l_{\rm C}} n_{\rm MT} - \frac{f l_{\rm He}}{L + f l_{\rm C}} n_{\rm C} = \rho_{\rm He} l_{\rm He} \sigma_{\rm He}, \tag{1.37}$$

where $n'_{\rm 12C}$ is the rate from the Carbon nucleus only and $n'_{\rm He}$ is the rate from liquid Helium only. The length and densities are listed in Table 1.6.

We need to establish how the rate from the Carbon target is related to the rate from the N^{15} in NH_3 and ND_3. The cross section for N^{15} can be written in terms of the cross sections on C^{12} ($\sigma_{\rm 12C}$) and on a bound neutron in N^{15} ($\sigma'_{\rm n}$).

$$\sigma_{15N} \approx \frac{7}{6} \sigma_{\rm 12C} + \sigma'_{\rm n} = \left(\frac{7}{6} + \frac{\sigma'_{\rm n}}{\sigma_{\rm 12C}} \right) \sigma_{\rm 12C}. \tag{1.38}$$

It is assumed that when the scattering occurs on protons inside the target material, the ratio of $\frac{\sigma'_n}{\sigma_{12C}} = 0$ and when the reaction happens on neutrons inside the target, the value of the ratio is $\frac{\sigma'_{\rm n}}{\sigma_{\rm 12C}} = \frac{1}{6}$, because there are six

bound neutrons in C^{12} [9].

Using the above quantities, the background represented by the number of counts due to the non-hydrogen and non-deuterium parts of the ammonia target can be expressed as

$$\begin{aligned} n_{\mathrm{B}} &= \left[\frac{\rho_{\mathrm{A}} l_{\mathrm{A}}}{\rho_{\mathrm{C}} l_{\mathrm{C}}}\left(\frac{7}{6}+\frac{\sigma'_{\mathrm{n}}}{\sigma_{12\mathrm{C}}}\right)+f\right] n'_{12\mathrm{C}} + (L-l_{\mathrm{A}}) n'_{4\mathrm{He}} \\ &= n_{\mathrm{MT}} + l_{\mathrm{A}}\left[\frac{\rho_{\mathrm{A}}}{\rho_{\mathrm{C}} l_{\mathrm{C}}}\left(\frac{7}{6}+\frac{\sigma'_{\mathrm{n}}}{\sigma_{12\mathrm{C}}}\right) n'_{12\mathrm{C}} - n'_{4\mathrm{He}}\right]. \end{aligned} \tag{1.39}$$

The dilution factor d_{f} is

$$d_{\mathrm{f}} = \frac{n_{\mathrm{A}} - n_{\mathrm{B}}}{n_{\mathrm{A}}}. \tag{1.40}$$

The dilution factor is compared below in Table 1.8:

Item	Description	Value
$\rho_{\mathrm{F}} l_{\mathrm{F}}$	Density times target length for empty target.	Al: 167 μm; 0.045 g/cm^2. Kapton: 384 μm; 0.055 g/cm^2. Total=Al + Kapton=0.0996 g/cm^2
$\rho_{\mathrm{C}} l_{\mathrm{C}}$	Density times target length for Carbon target.	0.498 g/cm^2
f	The ratio of counts from foils to the C^{12} slab in the Carbon target.	0.200
ρ_{He}	He density.	0.145 g/cm^3
L	The length of the target cell from the entrance to exit foil.	1.90 cm
ρ_{C}	C^{12} density.	2.17 g/cm^3
l_{C}	Carbon target length.	0.23 cm
$\rho_{\mathrm{NH_3}}$	NH_3 density	0.917 g/cm^3
$\rho_{\mathrm{ND_3}}$	ND_3 density	1.056 g/cm^3
l_{A}	Ammonia target length.	0.6 cm

Table 1.6: Length and density values for different types of target material reproduced from the EG1b experiment [9].

The fractional energy of the observed final state hadron(z)	Dilution Factor(d_{f})
NH_3, π^+ && $z = 0.4$	0.160 ± 0.02
NH_3, π^+ && $z = 0.7$	0.152 ± 0.03

Table 1.7: Calculated dilution Factor for NH_3 target type.

Reaction	Dilution Factor(d_{f})
Resonance region	0.11 - 0.13
Inclusive	0.14 - 0.17
Semi-Inclusive	0.122 - 0.182

Table 1.8: Dilution Factor compared with other results [8] [10].

Chapter 2

Results

2.1 Semi-Inclusive Pion Asymmetries

The final results are presented in this chapter. They have been obtained by analyzing the data collected in 2000 - 2001 at Thomas Jefferson National Laboratory using a longitudinally polarized electron beam on longitudinally polarized Hydrogen ($^{15}NH_3$) and Deuterium ($^{15}ND_3$) targets. The incident electron's energy was 4.2 GeV. The CEBAF Large Acceptance Spectrometer (CLAS) was used for particle detection. The measurements were made for the kinematic region where $x_B \geq 0.3$ and momentum transfer squared (Q^2) was 1.1 $\pm$ 0.2 GeV^2. The SIDIS asymmetries were measured at four different values of x_B and are presented on Figure 2.1.

2.2 Systematic Errors

The results presented in the previous sections include only statistical uncertainties. However, the experimental setup and the cuts used for particle identification and background elimination are sources of systematic errors. This section describes the methods used for estimating the systematic errors from each type of source. The systematic errors for the SIDIS asymmetries are shown

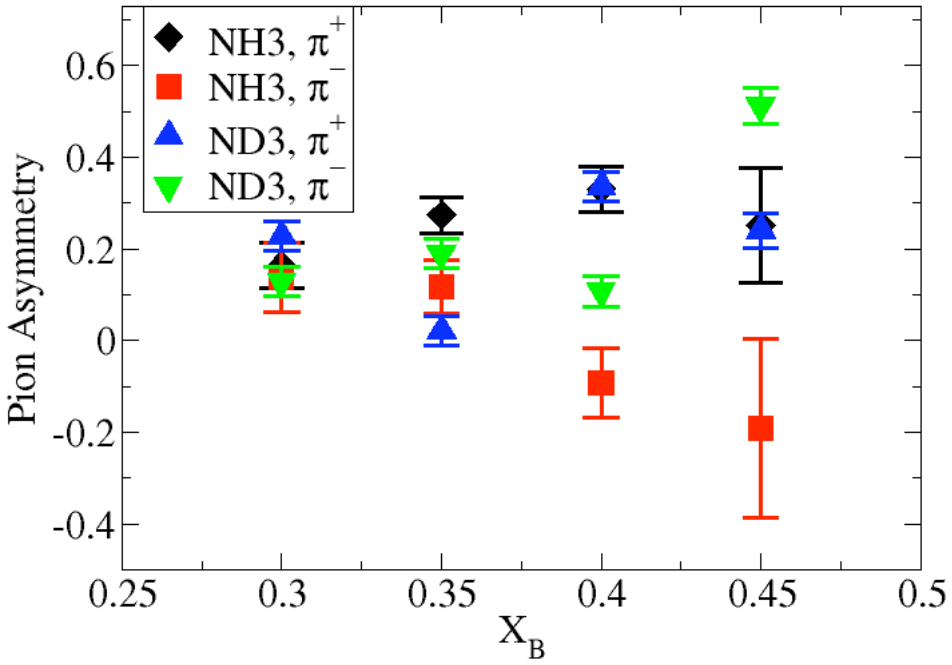

Fig. 2.1: x_B versus SIDIS pion asymmetries.

in Table 2.1. The total systematic error is calculated by combining individual systematic errors in quadrature.

Source	Systematic Error
Geometrical and timing cuts	1.40×10^{-2}
Electromagnetic calorimeter cut	3.50×10^{-2}
Dilution Factor	1.87×10^{-2}
Target and beam polarization	0.64×10^{-2}
Total	4.26×10^{-2}

Table 2.1: Summary of the systematic errors for the $A^{\pi^+}_{NH_3}$ asymmetry.

2.2.1 Cut Dependence

The systematic errors associated with the electromagnetic cuts and fiducial cuts for electron identification were calculated by comparing the SIDIS asymmetries before and after cuts were applied. As can be seen, the effect due to the electromagnetic calorimeter and fiducial cuts is on the order of 3.5 % and 1.4% respectively (Figure 2.2).

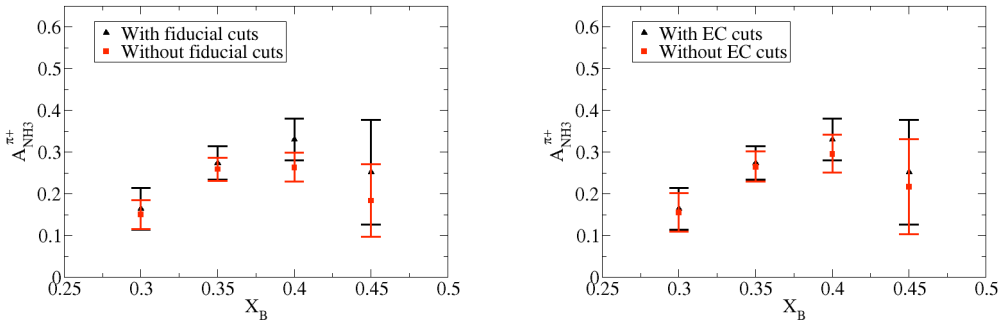

(a) (b)

Fig. 2.2: x_B versus $A_{\mathrm{NH3}}^{\pi^+}$ SIDIS asymmetry: (a) geometrical and timing cuts, (b) electromagnetic calorimeter cuts.

2.2.2 Dilution factor

Systematic effects related to the dilution factor were estimated the following way: First, the SIDIS asymmetries were calculated for the standard values of the dilution factor. Then asymmetries were recalculated by changing the value of each parameter by the amount of its uncertainty. The difference between these two values is the systematic effect due to the dilution factor. The resulting shift is about 1.9% (Figure 2.3).

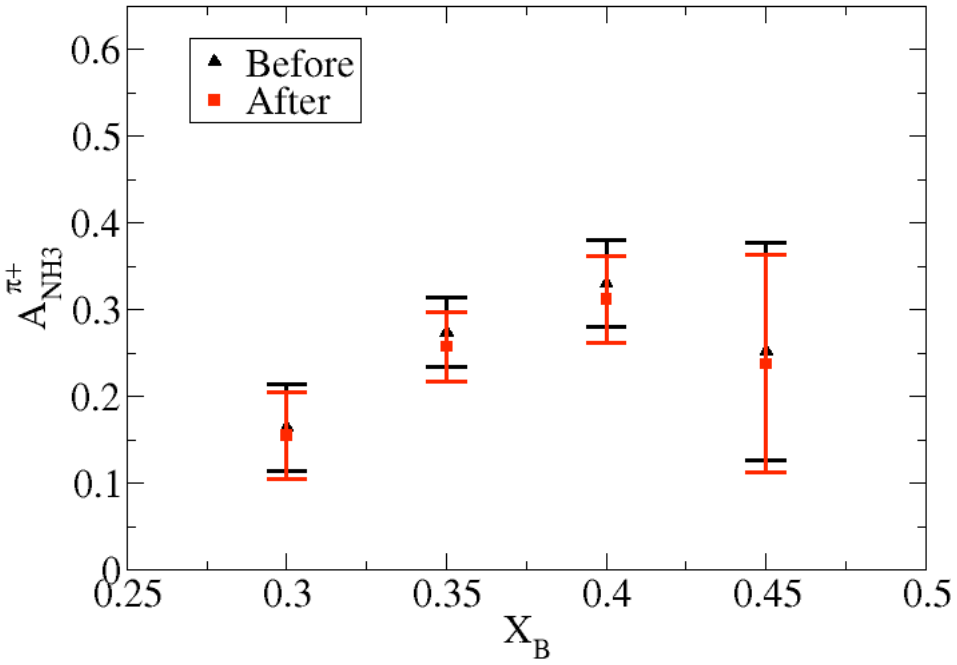

Fig. 2.3: x_B versus $A_{\mathrm{NH3}}^{\pi^+}$ SIDIS asymmetry.

2.2.3 Polarization

Systematic effects due to the target and beam polarization were estimated the following way: First, the SIDIS asymmetries were calculated for the standard values of the $\mathrm{P}_t \times \mathrm{P}_b$ polarization. Then asymmetries were recalculated by changing the value of each parameter by the amount of its uncertainty. The difference between these two values is the systematic error associated with the target and beam polarization, which is approximately 0.6% (Figure 2.4).

$$A_{\mathrm{meas}} = \frac{A_{\mathrm{raw}}}{\mathrm{P}_t \times \mathrm{P}_b}, \tag{2.1}$$

$$\delta A_{\rm meas}^{\rm syst} = \frac{\delta({\rm P}_t \times {\rm P}_b)^{\rm syst}}{{\rm P}_t \times {\rm P}_b} \frac{A_{\rm raw}}{{\rm P}_t \times {\rm P}_b} = 0.6\% \frac{A_{\rm raw}}{{\rm P}_t \times {\rm P}_b}. \tag{2.2}$$

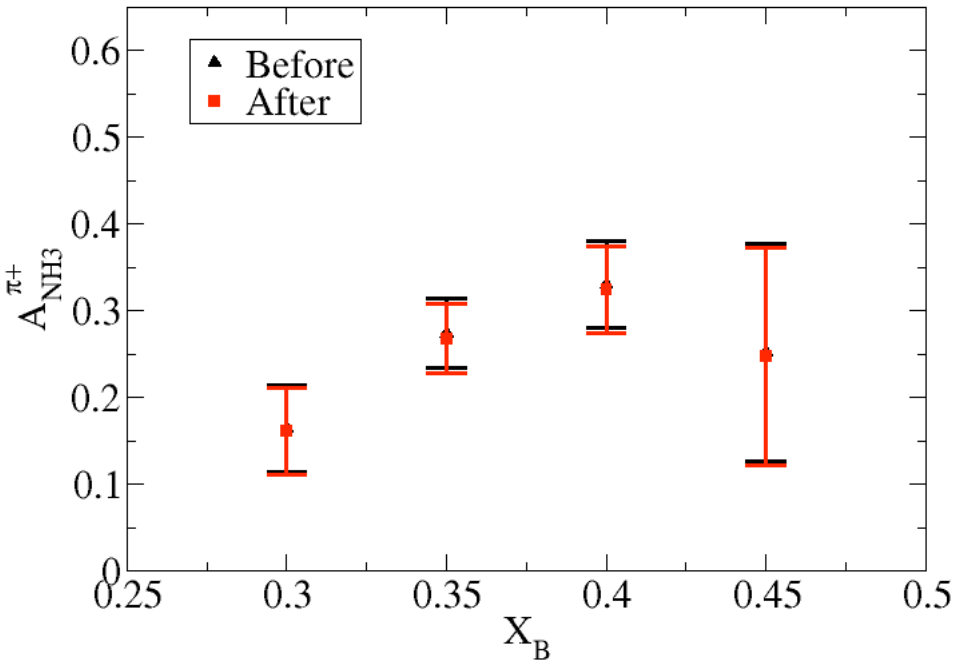

Fig. 2.4: x_B versus $A_{\rm NH3}^{\pi^+}$ SIDIS asymmetry.

2.3 Semi-Inclusive Pion Asymmetries

The corrected measured semi-inclusive deep inelastic asymmetries $A_{\rm NH3}^{\pi^+}$, $A_{\rm NH3}^{\pi^-}$, $A_{\rm ND3}^{\pi^+}$ and $A_{\rm ND3}^{\pi^-}$ are shown below on Figure 2.5 and compared to the asymmetries measured by the HERMES experiment. The SIDIS asymmetries for longitudinally polarized Hydrogen ($^{15}NH_3$) and Deuterium ($^{15}ND_3$) targets are listed in Table 2.2 for four values of x_B. The asymmetries have been cor-

rected for the target and beam polarization [11] and dilution factor from ref[12].

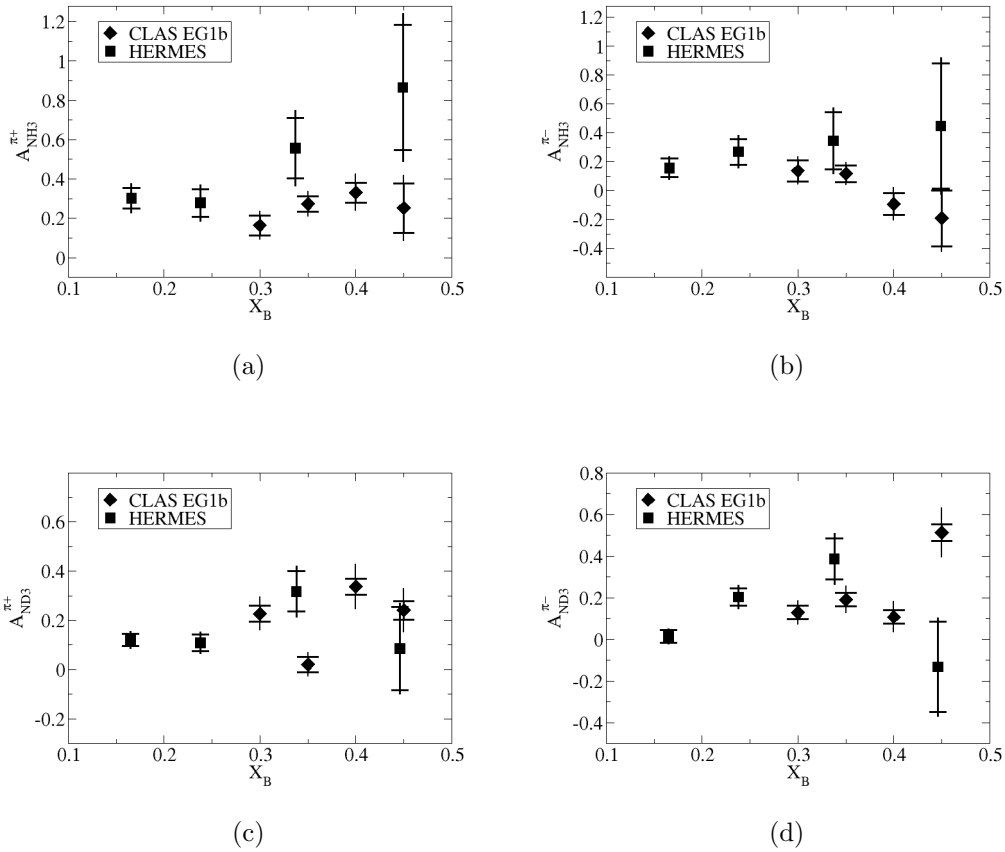

Fig. 2.5: x_B versus SIDIS asymmetry: (a) $A_{\mathrm{NH3}}^{\pi^+}$, (b) $A_{\mathrm{NH3}}^{\pi^-}$ (c) $A_{\mathrm{ND3}}^{\pi^+}$ and (d) $A_{\mathrm{ND3}}^{\pi^-}$. The solid black squares are measurements from ref[13] and the solid black diamonds represent SIDIS asymmetries measured using the data collected during the EG1b experiment. The error bar lines represent systematic uncertainty and the risers statistical uncertainty.

x_B	$A^{\pi^+}_{\mathrm{NH3}} \pm stat. \pm syst.$	$A^{\pi^-}_{\mathrm{NH3}} \pm stat. \pm syst.$
0.30	$0.1644 \pm 0.0504 \pm 0.0191$	$0.1378 \pm 0.0745 \pm 0.0183$
0.35	$0.2733 \pm 0.0400 \pm 0.0229$	$0.1183 \pm 0.0583 \pm 0.0176$
0.40	$0.3308 \pm 0.0499 \pm 0.0407$	$-0.0917 \pm 0.0753 \pm 0.0361$
0.45	$0.2521 \pm 0.1257 \pm 0.0387$	$-0.1908 \pm 0.1942 \pm 0.0374$
x_B	$A^{\pi^+}_{\mathrm{ND3}} \pm stat. \pm syst.$	$A^{\pi^-}_{\mathrm{ND3}} \pm stat. \pm syst.$
0.30	$0.2273 \pm 0.0317 \pm 0.0351$	$0.1286 \pm 0.0320 \pm 0.0240$
0.35	$0.0209 \pm 0.0314 \pm 0.0164$	$0.1904 \pm 0.0319 \pm 0.0306$
0.40	$0.3368 \pm 0.0322 \pm 0.0583$	$0.1080 \pm 0.0330 \pm 0.0386$
0.45	$0.2408 \pm 0.0377 \pm 0.0485$	$0.5125 \pm 0.0392 \pm 0.0787$

Table 2.2: Semi-inclusive asymmetries on the proton and deuterium targets ($A^{\pi^+,\pi^-}_{\mathrm{NH3}}$ and $A^{\pi^+,\pi^-}_{\mathrm{ND3}}$).

Bibliography

[1] B. Mecking *et. al.*, (The CLAS Collaboration), Nucl. Instr. Meth. A**503/3**, 513-553 (2003).

[2] M. Osipenko, A. Vlassov and M. Taiuti, *Matching between the electron candidate track and the Cherenkov counter hit*. CLAS-NOTE 2004-020 (2004).

[3] K. Nakamure *et. al.*, The Review of Particle Physics. Particle Data Group. J. Phys. G **37**, 075021 (2010).

[4] C. Lanczos, SIAM Journal of Numerical Analysis, B**1**, 86 (1964).

[5] K. Park, V. D. Burkert and W. Kim (The CLAS Collaboration), Phys. Rev. C**77**, 015208 (2008).

[6] J. Pierce, *Pion Identification code*,
From EG1 Hall-B, WWW Document,
(http://www.jlab.org/Hall-B/secure/eg1/EG2000/josh/pion.cc).

[7] Unitary Isobar Model, MAID2007, WWW Document,
(http://wwwkph.kph.uni-mainz.de/MAID//maid2007/maid2007.html).

[8] R. G. Fersch, *Measurement of Inclusive Proton Double Spin Asymmetries and polarized Structure Functions*. Doctoral dissertation. The College of William and Mary, Williamsburg, VA (2008).

[9] S. E. Khun, *Dilution Factor for Exclusive Channels*. Old Dominion University, Norfolk, VA (2010).

[10] Y. A. Prok, *Measurement of The Spin Structure Function $g_1(x, Q^2)$ of the Proton in The Resonance Region*. Doctoral dissertation. University of Virginia, Richmond, VA, 2004.

[11] K. V. Dharmawardane *et. al.*, (The CLAS Collaboration), Phys. Lett. **B641**, 11 (2006).

[12] P. Bosted *et. al.*, *Interpolated model calculated dilution factors for EG1b directly from radiated cross-sections*, WWW Document, (http://www.jlab.org/Hall-B/secure/eg1/EG2000/fersch/DILUTION/dilutionmodel/) (2007).

[13] A. Airapetian *et. al.*, (The HERMES Collaboration), Phys. Rev. Lett. 92, 012005 (2004).